Melting and refreezing of porous media

Sudip S. Dosanjh
Reactor Safety Theoretical Physics Division, Sandia National Laboratories, Albuquerque, NM, USA

During severe nuclear reactor accidents similar to Three-Mile Island, the fuel rods can fragment and thus convert the reactor core into a large rubble bed composed primarily of UO_2 and ZrO_2 particles. In the present study a one-dimensional model is developed for the melting and refreezing of such a bed. The analysis includes mass conservation equations for the species of interest (UO_2 and ZrO_2); a momentum equation that represents a balance among drag, capillary and gravity forces; an energy equation that incorporates the effects of convection by the melt, radiation and conduction through the bed and internal heat generation; and a UO_2-ZrO_2 phase diagram. A few key results are that (1) capillary forces are only important in beds composed of particles smaller than a few millimeters in diameter and in such beds, melt relocates both upward and downward until it freezes, forming crusted regions above and below the melt zone; (2) as melt flows downward and freezes, a flow blockage forms near the bottom of the bed and the location of this blockage is determined by the bottom thermal boundary layer thickness; (3) the maximum thickness of the lower crust increases linearly with the height of the bed; and (4) deviations from initially uniform composition profiles occur because ZrO_2 is preferentially melted and these deviations decrease as the initial ZrO_2 concentration is increased.

Keywords: heat and mass transfer; porous media; melting; freezing

Introduction

During severe nuclear reactor accidents similar to Three-Mile Island, the fuel rods can fragment and thus convert the reactor core into a large debris bed composed primarily of UO_2 and ZrO_2 particles.[1] As energy is released by fission product decay, liquid coolant in the bed can boil away and temperatures in the bed can eventually surpass the UO_2-ZrO_2 melting point (2800 K).[2] Of interest to this study are heat transfer and melt propagation in the bed after the particle bed becomes dry (here, dry refers to the absence of liquid coolant).

Liquid/gas phase changes in porous media have received considerable attention in the literature.[3–9] Researchers have developed one-dimensional models for the evaporation and condensation of water in a variety of materials: porous insulation,[3] concrete,[4,5] brick,[6] wood,[6,7] and reactor materials.[8] In these studies the porous solid did not participate in the phase change phenomenon; however, its presence did significantly affect fluid motion. Ogniewicz and Tien[3] as well as Sahota and Pagni[4] assumed that the liquid was immobile: this can occur because the liquid is trapped between the particles by surface tension for low values of the saturation (the fraction of nonsolid volume filled with liquid). Nasrallah and Perre,[6] Plumb *et al.*,[7] and Lipinski[8] used modified versions of Darcy's law to account for the simultaneous motion of vapor and liquid.

Sublimation and freezing were modeled by Fey and Boles[10] who studied the self-freezing of an initially wet, semi-infinite bed. Energy equations were solved in each of three regions (dried, frozen, and wet) considered by their model whereas mass transfer was analyzed in the dry region only. Solid/liquid phase change processes in porous media were also scrutinized by Weaver and Viskanta,[11] Chellaiah and Viskanta,[12] as well as by Beckermann and Viskanta:[13] two materials were present in the problems they considered (a fixed porous matrix, usually composed of glass beads, and a phase change material that existed in either the solid or the liquid state). In all of these studies[10–13] it was assumed that melting/freezing occurred in a thin, sharply defined phase change interface and at most two phases existed simultaneously in any given region.

In the present study solid/liquid phase changes are of interest and three phases (solid, liquid, and gas) are present simultaneously. A schematic of the problem of interest is shown in Figure 1. Solid melts in the center of a dry bed resulting in the formation of a voided region with a porosity ε which is larger than the initial porosity ε_i. Molten materials relocate under the action of gravity and capillary forces and subsequently freeze in colder regions near the boundaries of the bed.[14] Crusts with porosities lower than the initial porosity (i.e., $\varepsilon < \varepsilon_i$) form above and below the melt zone. As happened at Three-Mile Island,[1] liquid accumulates above the lower crust forming a molten pool.

A one-dimensional melt propagation model is developed in this study and the effects of varying the particle diameter, composition, bed height and initial conditions are discussed. The equations governing melt relocation are similar to the undersaturated flow equations given by Scheidegger.[15] The primary differences are that in the present study source terms are needed in the mass conservation equations to account for phase changes and an energy equation (with an associated phase diagram) must be solved to determine the temperature increase of the bed and the rate of melting and freezing.

Analysis

Mathematical formulation

The following assumptions are employed in the current analysis:

(1) The average particle diameter, d_p, is taken to be much smaller than the distance characteristic of macroscopic changes in temperature and species concentrations, x_c. Therefore, the

Address reprint requests to Dr. Dosanjh at the Reactor Safety Theoretical Physics Division, Sandia National Laboratories, Albuquerque, NM 87185, USA.

Received 15 October 1988; accepted 18 February 1989

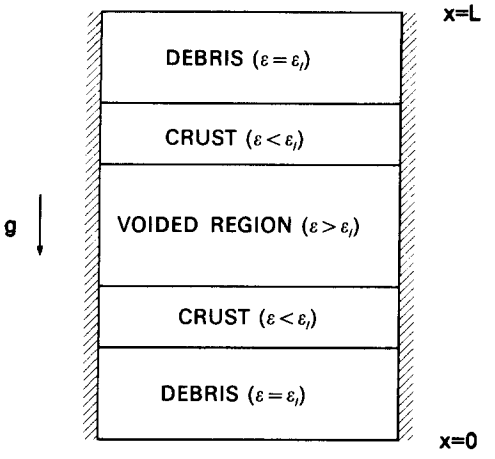

Figure 1 Schematic of melt formation and relocation in a one-dimensional debris bed. The local porosity ε is the volume fraction occupied by liquid and gas and the subscript *i* refers to initial value

microscopic governing equations can be volume averaged to yield macroscopic porous medium equations.

(2) A linear version of Darcy's law can be used for the liquid momentum equation. Inertial terms are neglected and it is assumed that the Reynolds number based on particle diameter, Re_p, is small. ($Re_p = qd_p/\nu$, where q is the liquid velocity and ν is the kinematic viscosity.)

(3) Movement of the gas has a negligible effect on the motion of the liquid and heat transfer. This is a reasonable assumption in the applications of interest because typical gas velocities are low, on the order of 0.01 m/s.[16]

(4) Radiation heat transfer through the bed can be modeled using a temperature dependent thermal conductivity.

(5) The solid and the liquid are in local thermal equilibrium and consequently, only one energy equation must be solved.

(6) The melt is incompressible.

(7) The vapor pressures of the materials of interest are sufficiently low that evaporation and condensation can be neglected.

(8) On the particle scale the species are well mixed and the UO_2-ZrO_2 phase diagram given by Hagrman[17] can be used. This assumption implies that $d_p \ll [D\tau_c]^{1/2}$, where D is a UO_2-ZrO_2 diffusion coefficient and τ_c is the time scale of interest (e.g., the time associated with the heat-up of the bed). Furthermore, it is assumed that species diffusion can be neglected over length scales comparable to the characteristic distance x_c—that is, $[D\tau_c]^{1/2} \ll x_c$. In summary, we assume that $d_p \ll [D\tau_c]^{1/2} \ll x_c$.

(9) Properties remain fixed at constant values, although the properties of different materials may differ.

In addition, it is assumed that the particles remain fixed in space as they melt. This assumption is clearly not valid at extremely high porosities. However, scoping experiments[14] conducted in a research reactor indicate that the particles do not start settling downward until the porosity surpasses a value of about 0.7. As the solid melts, some fraction of the liquid is trapped near the contact points between particles by surface tension forces. These surface tension forces also tend to hold the particles in place. When the particles eventually start moving, the analysis presented in this paper breaks down and consequently, results presented here are only valid until the porosity reaches a value of 0.7.

Using the above assumptions the one-dimensional model consists of the following equations:

Conservation of mass. Balancing the liquid mass stored in a differential control volume, the convective flux flowing into this volume and production/depletion by melting/freezing gives for species j ($j=1$ and $j=2$ correspond to UO_2 and ZrO_2, respectively):

$$\frac{\partial}{\partial t}[Y_{lj}\rho_{lj}\varepsilon S] + \frac{\partial}{\partial x}[Y_{lj}\rho_{lj}q] = -\frac{\partial}{\partial t}[Y_{sj}\rho_{sj}(1-\varepsilon)] \tag{1}$$

where the subscripts l and s refer to liquid and solid, respectively. The local porosity ε is the volume fraction occupied by liquid and gas, the saturation S is the fraction of the porosity that is filled with liquid, q is a superficial velocity, ρ_{ij} is the density of species j in phase i, and Y_{ij} is the fraction of phase i that is occupied by species j. The Y_{ij}'s are related to each other by $Y_{l1} + Y_{l2} = 1$ and $Y_{s1} + Y_{s2} = 1$.

Conservation of momentum. Balancing viscous drag forces, which are assumed to vary linearly with q, changes in pressure

Notation

- c_p Specific heat, J/kg-K
- d_p Particle diameter, mm
- D Mass diffusivity, m^2/s
- g Gravitational acceleration, m/s^2
- h Enthalpy, J/kg
- h_f Heat of fusion, J/kg
- H Local total enthalpy, J/m^3
- J Leverett function
- k Thermal conductivity, W/m-K
- L Bed height, m
- P_c Capillary pressure, N/m^2
- P_g Gas pressure, N/m^2
- P_l Liquid pressure, N/m^2
- q Superficial liquid velocity, m/s
- Q Decay heat, W/kg of UO_2
- S Saturation (fraction of porosity ε occupied by liquid)
- S_e Effective saturation, $S_e = (S - S_r)/(1 - S_r)$
- S_r Residual saturation (critical value of S below which liquid motion ceases)
- t Time, s
- T Temperature, K
- x Distance from the bottom of the bed, m
- Y_{lj} Volume of liquid species j/volume of the liquid
- Y_{sj} Volume of solid species j/volume of the solid

Greek

- α_s Thermal diffusivity, m^2/s
- γ Surface tension, N/m
- ε Porosity (volume fraction occupied by liquid and gas)
- ε_r Emissivity
- κ Permeability, m^2
- μ Viscosity, Pa-s
- ρ_{lj} Density of liquid species j, kg/m^3
- ρ_{sj} Density of solid species j, kg/m^3

Subscripts

- g gas
- l liquid
- s solid

and gravity gives:

$$\frac{\mu}{\kappa_l} q = -\frac{\partial}{\partial x} P_l - g\rho_l \tag{2}$$

where μ is the dynamic viscosity of the liquid, g is the gravitational acceleration and κ_l is the relative permeability. Equation 2 is similar to the traditional form of Darcy's law: the only difference is that the permeability κ defined in Bird *et al.*[18] is replaced by a relative permeability κ_l to account for the presence of three phases (solid, liquid, and gas). Typically, κ_l depends on the particle diameter, d_p, the porosity, ε, the saturation, S, and a critical value of the saturation, S_r, that is often referred to as the residual saturation.[15] The quantity S_r is defined as the threshold value of saturation below which bulk liquid motion ceases. For $S < S_r$, $\kappa_l = 0$ and Equation 2 requires that $q = 0$. When the saturation is less than the critical value, the liquid is trapped between the particles by surface tension effects.[19] Liquid starts to flow when the saturation is increased to the point that these pockets of trapped liquid touch and coalesce.[19] At the other extreme, as the saturation approaches 1, κ_l approaches κ. That is, when S equals 1 only two phases are present (solid and liquid) and the relative permeability must equal the permeability given by Bird *et al.*[18] for the flow of a single fluid through a porous matrix.

Capillary forces enter Equation 2 through the term involving the liquid pressure, P_l. The capillary pressure is defined as the difference between P_l and the gas pressure, P_g (that is, $P_c = P_g - P_l$).[15,19] This difference arises because of surface tension effects: that is, the capillary pressure is zero in systems of zero surface tension. In the applications of interest, gas velocities are low, the gas pressure changes by a small amount and the pressure gradient term in Equation 2 can be replaced using $\partial P_l/\partial x = -\partial P_c/\partial x$. From Equation 2 it is therefore evident that capillary forces move liquid into regions of high P_c. Using dimensional analysis Leverett[19] concluded that the capillary pressure is given by $P_c = J\gamma(\varepsilon/\kappa)^{1/2}$, where γ is the surface tension and J is an empirically determined function of the effective saturation, $S_e = (S - S_r)/(1 - S_r)$. As the particle diameter increases, κ increases[18] and P_c decreases. Consequently, capillary forces are small in beds with large particles. Decreasing ε increases both ε/κ[18] and P_c and, consequently, capillary forces tend to move liquid into regions of lower porosity. This behavior is similar to the classical capillarity demonstration discussed by Batchelor[20] in which liquid is observed to rise in a small diameter tube when the tube is inserted into an infinite liquid pool.

Correlations for κ_l, κ, S_r, and J are given in the appendix. It is worth noting that S_r varies with the ratio of surface tension forces to gravity and that decreasing the particle diameter or the porosity raises S_r.[21] Therefore, the saturation must be increased to a high value before macroscopic liquid motion is observed in packed beds consisting of small, tightly packed particles.

Conservation of energy. Balancing the energy stored in the solid and the liquid, convection, diffusion and internal heat generation, gives:

$$\frac{\partial}{\partial t}\sum_j [(1-\varepsilon)Y_{sj}\rho_{sj}h_{sj} + \varepsilon S Y_{lj}\rho_{lj}h_{lj}] + \frac{\partial}{\partial x} q \sum_j Y_{lj}\rho_{lj}h_{lj}$$
$$= \frac{\partial}{\partial x} k_{\text{eff}} \frac{\partial T}{\partial x} + [(1-\varepsilon)\rho_{s1} Y_{s1} + \varepsilon S \rho_{l1} Y_{l1}]Q \tag{3}$$

where h_{ij} is the enthalpy of species j in phase i and Q is the energy released by fission product decay per mass of UO_2 (a correlation for k_{eff} is given in the appendix). An enthalpy formulation for the energy equation is used to account for phase changes. In the problem of interest to this study, temperatures increase uniformly and the solid can melt over a large fraction of the bed simultaneously (consequently, an interface approach cannot be used).

Table 1 Typical initial properties of a core rubble bed

Quantity of interest	Typical value
Decay heat, Q [W/kg of UO_2]	300.0
Height of bed, L [m]	1.0
Particle diameter, d_p [mm]	0.1–10.0
Porosity, ε	0.4
UO_2 solid volume fraction, Y_{s1}	≥ 0.64
ZrO_2 solid volume fraction, Y_{s2}	≤ 0.36

Closure

In order to solve the preceding set of equations, the decay heat, initial species volume fractions, a phase diagram, an initial temperature distribution, boundary conditions and properties must be specified. Typical characteristics of a UO_2-ZrO_2 core rubble bed similar to the one found in Three-Mile Island[1] are given in Table 1. One hour after reactor shutdown, power generation falls to approximately 1% of peak power.[22] A TMI-2 type plant with an operating power of 2.8×10^3 MW and 93,000 kg of UO_2 (Ref. 23) in the core has a decay heat Q on the order of 300 W/kg of UO_2. Because it takes several days for the decay heat to decrease significantly below the one-hour value,[22] it is assumed constant in the following analysis. An upper limit for the ZrO_2 volume fraction Y_{s2} is estimated by assuming that all of the roughly 23,000 kg of Zr in a typical core[23] are oxidized, resulting in the formation of 30,000 kg of ZrO_2. Neglecting materials other than UO_2 and ZrO_2 gives a maximum ZrO_2 mass fraction of 0.25. Setting the solid densities of UO_2 and ZrO_2 equal to 10,000 and 5700 kg/m^3 (Refs. 17,24), respectively, gives a maximum ZrO_2 volume fraction Y_{s2} of 0.36.

The UO_2-ZrO_2 phase diagram given by Hagrman[17] is used. Solid starts melting when the temperature reaches the solidus temperature (the lower line) shown in Figure 2. (Note that the melting temperature varies with the composition of the system and consequently, phase changes can also occur by changing the composition and keeping the temperature fixed.)

An initial linear temperature profile is prescribed: $T(x, 0) = T_0 + (T_L - T_0)x/L$, where L is the height of the bed, T_0 is

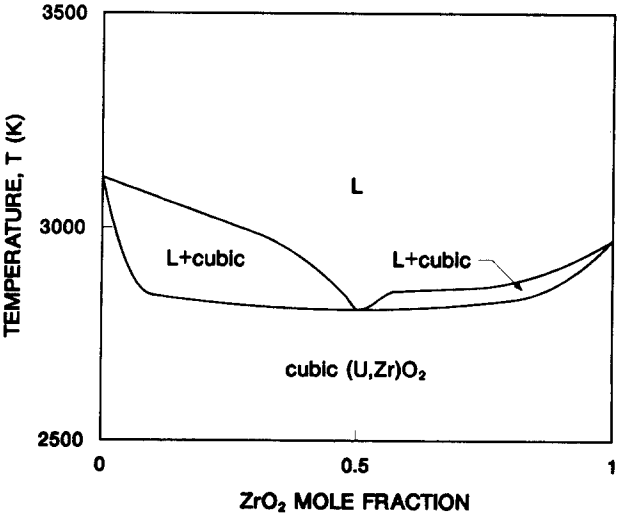

Figure 2 Phase diagram for UO_2-ZrO_2

Table 2 Typical UO_2 and ZrO_2 properties[17,24]

Property	UO_2	ZrO_2
Solid density, ρ_{si} [kg/m^3]	10,000	5,700
Liquid density, ρ_{lj} [kg/m^3]	9,000	5,700
Solid specific heat, c_{psj} [J/kg-K]	930	700
Liquid specific heat, c_{plj} [J/kg-K]	490	815
Solid thermal conductivity, k_{sj} [W/m-K]	3.0	2.0
Liquid thermal conductivity, k_{lj} [W/m-K]	5.5	2.7
Heat of fusion, h_{fj} [kJ/kg]	274	706
Viscosity, μ_j [mPa-s]	5.8	3.5
Surface tension, γ_j [N/m]	0.45	0.45

the temperature at the bottom ($x=0$) and $T_L(\geq T_0)$ is the temperature at the top ($x=L$). Top and bottom boundaries radiate to environments at T_L and T_0, respectively. Typical UO_2 and ZrO_2 properties are given in Table 2.

Solution algorithm

Equations 1 and 3 are solved using a time-explicit finite difference scheme in conjunction with a staggered grid method[25] in which temperatures and species volume fractions are determined at the primary grid points and velocities are calculated at locations between these points (this is equivalent to using computational cells and evaluating the velocities at cell boundaries). The time step is controlled in accordance with an approximate stability criterion and because liquid velocities are low, the convective terms in Equations 1 and 3 are calculated using central differencing. In the calculations presented in this study 50–100 grid points were needed to resolve temperature and species gradients in the bed.

Solution of Equations 1–3 is somewhat complicated by the fact that time derivatives appearing in these equations involve products of the primitive variables, T, ε, S, Y_{s1}, Y_{s2}, Y_{l1}, and Y_{l2}. Given the values of all variables at a time step n, the solution algorithm is as follows. The velocity field is calculated at cell boundaries utilizing Equation 2 and information at step n. Next, the bulk densities (which are based on total volume) of UO_2 and ZrO_2,

$$\tilde{\rho}_{UO_2}=(1-\varepsilon)Y_{s1}\rho_{s1}+\varepsilon S Y_{l1}\rho_{l1} \tag{4}$$

and

$$\tilde{\rho}_{ZrO_2}=(1-\varepsilon)Y_{s2}\rho_{s2}+\varepsilon S Y_{l2}\rho_{l2} \tag{5}$$

respectively, and the enthalpy function,

$$H=\sum_{j=1}^{2}[(1-\varepsilon)Y_{sj}\rho_{sj}h_{sj}+\varepsilon S Y_{lj}\rho_{lj}h_{lj}] \tag{6}$$

are calculated at time step $n+1$ at the center of each calculation cell from Equations 1 and 3—convection and diffusion terms in these equations are evaluated explicitly using information at step n. When only one phase is present, solution of Equations 4–6 is straightforward. In two phase regions a phase diagram provides additional relations of the form

$$\frac{Y_{s2}\rho_{s2}/M_2}{\sum_{j=1}^{2}Y_{sj}\rho_{sj}/M_j}=f(T) \tag{7}$$

and

$$\frac{Y_{l2}\rho_{l2}/M_2}{\sum_{j=1}^{2}Y_{lj}\rho_{lj}/M_j}=g(T) \tag{8}$$

where M_j is the molecular weight of species j and f and g are specified functions of temperature. Terms on the left-hand sides of Equations 7 and 8 represent mole fractions of ZrO_2 in the solid and liquid phases, respectively. Equations 4–8 along with the relations, $Y_{s2}=1-Y_{s1}$ and $Y_{l2}=1-Y_{l1}$, are then solved for the primitive variables, T, ε, S, Y_{s1}, Y_{s2}, Y_{l1}, and Y_{l2}.

Order of magnitude analysis

Consider a debris bed with initial temperature and enthalpy profiles $T(x,0)$ and $H(x,0)$, respectively, where $T(x,0)$ is less than the melting temperature for all x. If the distance characteristic of changes in $T(x,0)$ is on the order of the height of the bed, L, and the boundaries radiate to cold environments as temperatures increase, then boundary information becomes important over the entire domain at time $t=L^2/\alpha_s$ (i.e., at this time, the conduction term in Equation 3 is important over the entire domain), where α_s is an average solid thermal diffusivity. Using the properties in Table 2, setting $\varepsilon=0.4$ and $k_{eff}=5\,W/m\cdot K$ gives $\alpha_s\simeq k_{eff}/[(1-\varepsilon)\rho_s c_{ps}]\simeq 10^{-6}\,m^2/s$. Rubble beds with heights on the order of 1 m heat up approximately adiabatically until time $L^2/\alpha_s\simeq 10^6$ s. For the times of interest, $T(x,t)$ is highly dependent on initial conditions and conduction and radiation are only important within boundary layers of thickness $\delta\simeq[\alpha_s t]^{1/2}$. Conduction is not important in the region $\delta\ll x\ll L-\delta$, and Equation 3 gives:

$$H(x,t)-H(x,0)=[(1-\varepsilon)Y_{s1}\rho_{s1}+\varepsilon S Y_{l1}\rho_{l1}]Qt \tag{9}$$

where the convective terms have been neglected (note from Equation 1 that the quantity in brackets in the right-hand side of Equation 9 remains constant in time if the convective terms in Equation 1 are neglected). Setting $Q=300$ W/kg of UO_2, $Y_{s1}=0.64$ and utilizing the properties in Table 2 gives 0.35 K/s as an approximate lower bound for the heating rate. For beds composed of only UO_2 particles ($Y_{s1}=1$), Equation 9 gives a heating rate of 0.5 K/s. Therefore, it takes between 2000 s and 2860 s for the temperature of the bed to increase by 1000 K. This simple theoretical model is valid until the melt starts relocating.

Results and discussion

Base case

Calculations are presented in this section for a particulate bed with a ZrO_2 to UO_2 mass ratio of 0.1, which corresponds to a ZrO_2 volume fraction of 0.15, an initial porosity ε of 0.4 and an average particle diameter d_p of 1 mm. An initial linear temperature profile is prescribed and the top and bottom of the bed radiate to environments with temperatures of 2000 K and 1500 K, respectively. Although spatially varying initial composition and porosity profiles can be prescribed, uniform initial conditions are chosen to simplify the interpretation of the results: this simplification is not expected to lead to large errors because the particle bed that formed in the Three-Mile Island reactor was fairly uniform.[1] The effects of varying the particle diameter, the bed height, the composition and the initial conditions are discussed in the next section.

Temperature profiles at 2300 s predicted by the complete theory and Equation 9, which is referred to by the term "simple theory," are shown in Figure 3. Solid has started to melt (note the change in slope at 0.35 m in Figure 3); however, at this time, the saturation is below the critical value, S_r, and the melt has not started relocating. As one would expect, predictions using Equation 9 are in excellent agreement with the full theory everywhere except in thermal boundary layers near the top and the bottom.

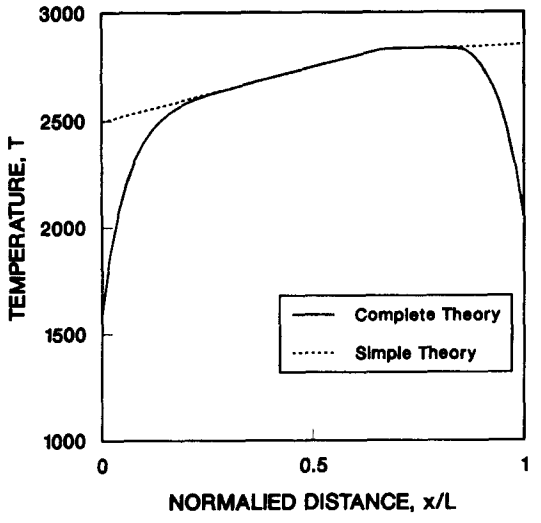

Figure 3 Temperature profiles at 2300 s predicted by the complete theory and a simple theoretical model that neglects conduction and liquid motion (for this calculation $L=0.5$ m)

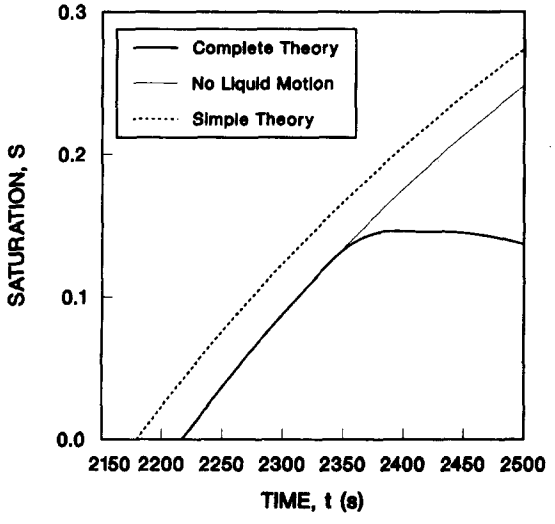

Figure 4 Saturation as a function of time at $x=0.4$ m, the location at which melt first forms. Results were obtained using the full theory (dark solid line), neglecting liquid motion (thin solid line) and neglecting both liquid motion and conduction (dashed line)

Time-dependent saturations at $x=0.4$ m, the point at which solid first melts, are plotted in Figure 4. Results shown in this figure were obtained (1) using the full theory (dark solid line); (2) neglecting liquid motion and setting $q=0$ in the energy equation (thin solid line); and (3) neglecting liquid motion and conduction, which gives the simple theoretical model discussed in the previous section (dashed line). Note that the inclusion of conduction delays melting by about 50 s. Because the top is the hottest initially, the top thermal boundary layer affects the timing of melting. On the other hand, liquid motion has no effect until $t\simeq 2350$ s. For $d_p=1$ mm and $\varepsilon=0.4$ the correlations in the appendix give $S_r\simeq 0.1$. In the complete theory, the saturation increases at approximately a constant rate until it surpasses the critical value, S_r; at this time, liquid starts flowing downward and as solid continues to melt, the saturation remains fixed at a constant value slightly higher than S_r.

Time-dependent porosities at $x=0.4$ m are shown in Figure 5. When liquid motion is neglected, the result is identical to the complete theory prediction in Figure 5. That is, liquid motion has very little effect on the rate at which the porosity changes (or equivalently, on the rate of melting). Note from Figure 5 that neglecting conduction displaces the porosity profiles about 50 s in time.

Temperature contours in space and time are shown in Figure 6. The 2800 K contour approximately represents the onset of melting. The temperature increases linearly with time in most of the bed until solid starts melting. That is, the initial linear temperature profile is preserved until $t=2200$ s. The change in temperature from 2600 K to 2800 K takes about 450 s in the region $0.25\text{ m}<x<0.4$ m. As x decreases, this 200 K temperature change occurs faster due to the downward flow of hot liquid.

Temperatures at $x=0.10$ m, $x=0.15$ m, and $x=0.20$ m are shown in Figure 7. Initially, the temperature increases linearly at the rate of 0.42 K/s. Arrival of the melt front is marked by a rapid increase in temperature to the melting temperature (2800 K)—melt flowing downward freezes upon reaching regions where the temperature is below the melt temperature, giving

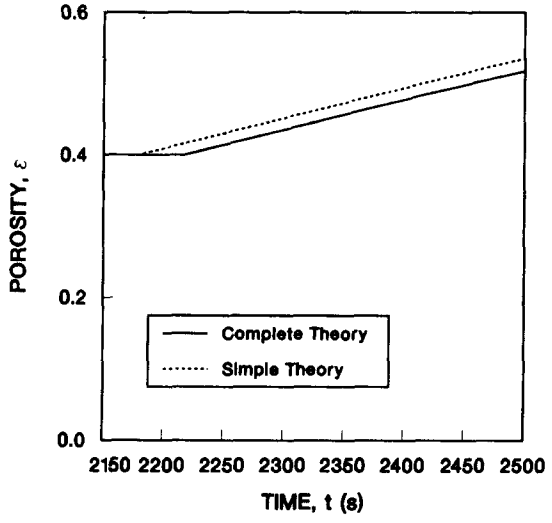

Figure 5 Porosity as a function of time at $x=0.4$ m, the location at which melt first forms, predicted by the full theory and a simple model that neglects liquid motion and conduction

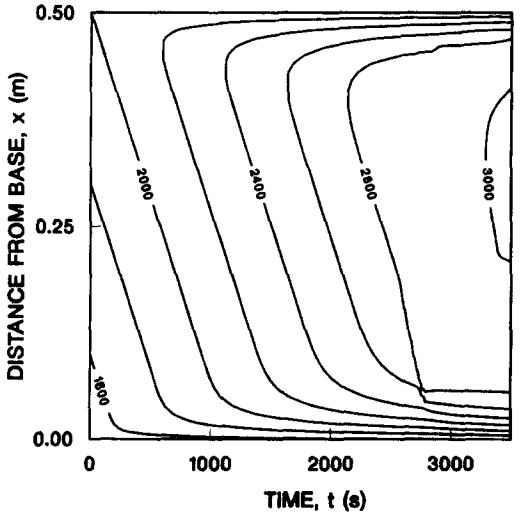

Figure 6 Temperature contours in space and time for the base case. Contours are shown every 200 K from 1600 K to 3000 K (for this calculation $L=0.5$ m)

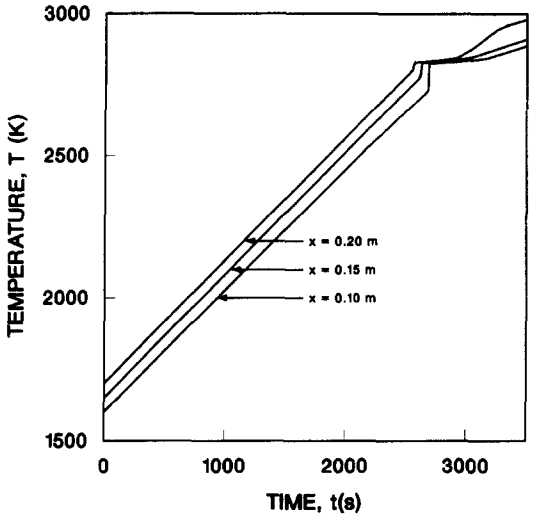

Figure 7 Temperature at $x=0.1$ m, $x=0.15$ m, and $x=0.2$ m as a function of time for the base case

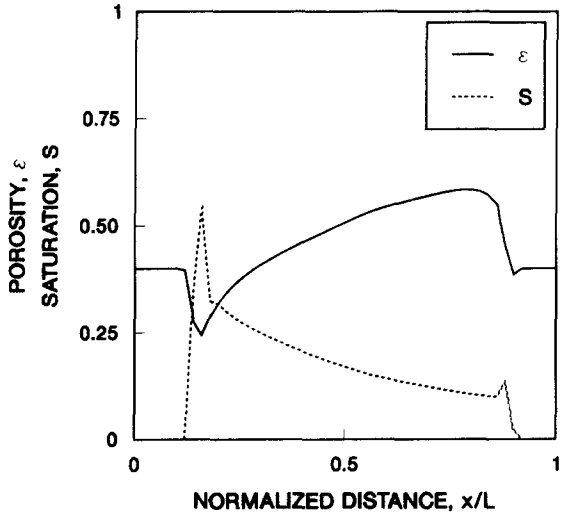

Figure 8 Porosity and saturation profiles at $t=2750$ s for the base case (for this calculation $L=0.5$ m)

up its heat of fusion and thus increasing the local temperature (and decreasing the local porosity). After the onset of melting, the temperature increase slows as most of the decay heat is used to melt the solid. Note from Figure 7 that the jump in temperature increases as x decreases, ranging from 30 K at $x=0.2$ m to 95 K at $x=0.1$ m. Therefore, in order to reach the melting temperature, a greater amount of liquid must freeze as one approaches the bottom of the bed. When the liquid front reaches the bottom thermal boundary layer, the heat of fusion is not sufficient to raise the local temperature to 2800 K. A complete blockage, corresponding to a porosity of 0.0, forms at this location.

Porosity, ε, and saturation, S, profiles at time $t=2750$ s are shown in Figure 8. As solid melts in the center of the bed, ε increases. Capillary forces, which tend to move liquid into regions of high capillary pressure (and low porosity), and gravity induce flow out of the central zone. Saturation increases near the bottom signifying considerable liquid motion downward. This is due to the fact that downward relocation is caused by both forces, while in the upward direction, capillary forces are opposed by gravity. Significant upward motion is only possible when capillary forces are several times larger than gravity. As evidenced by Figure 8, a small amount of liquid accumulates in the top of the melt zone in a bed with 1 mm diameter particles indicating that capillary and gravity forces are of the same order of magnitude. It will be shown in the next section that the capillary force plays a significant role in beds with particles smaller than 1 mm and is negligible in beds of larger particles. Note from Figure 8 that liquid flowing downward into colder portions of the bed has frozen, decreasing the local porosity below its initial value of 0.4. At $t=2750$ s, a 9-cm-thick crust has formed below the melt zone and an upper crust has just begun to form.

Porosity contours in space and time are shown in Figure 9. As evidenced by the appearance of the $\varepsilon>0.4$ region in Figure 9, melt first forms at $t=2215$ s and $x=0.4$ m. Melt starts flowing at 2310 s and a lower crust begins forming at 2510 s. Note the creation of a $\varepsilon<0.4$ zone in Figure 9. At 2780 s a blockage forms near the bottom of the bed and melt flowing downward subsequently accumulates in region B in Figure 9, creating a

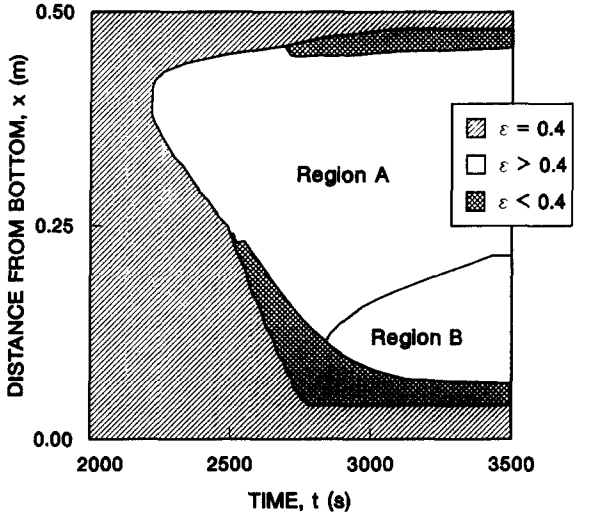

Figure 9 Schematic of crust growth for the base case. Region *A* consists of solid, liquid and gas while region *B* is composed of solid and liquid (that is, region *B* is filled with liquid). In region *A* the saturation S is near S_r while region *B* is fully saturated ($S=1$)

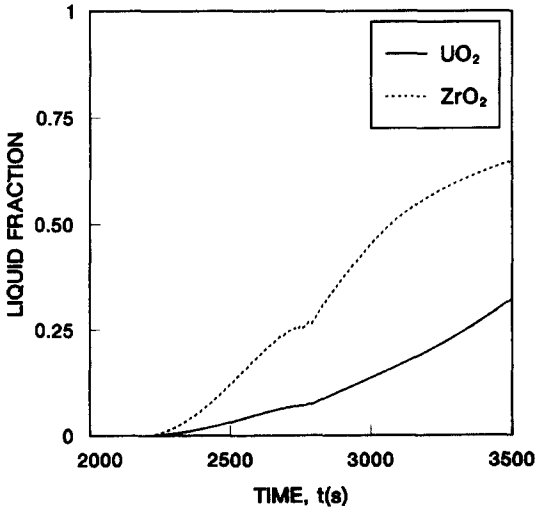

Figure 10 Fraction of UO_2 and ZrO_2 in the liquid as a function of time for the base case

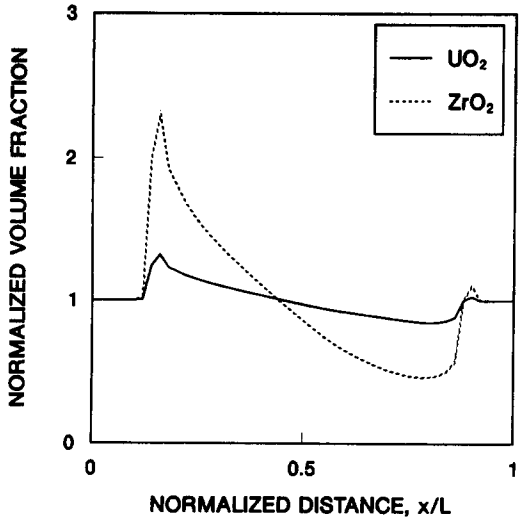

Figure 11 UO_2 and ZrO_2 volume fractions normalized by their initial (uniform) values at $t=3000$ s for the base case (for this calculation $L=0.5$ m)

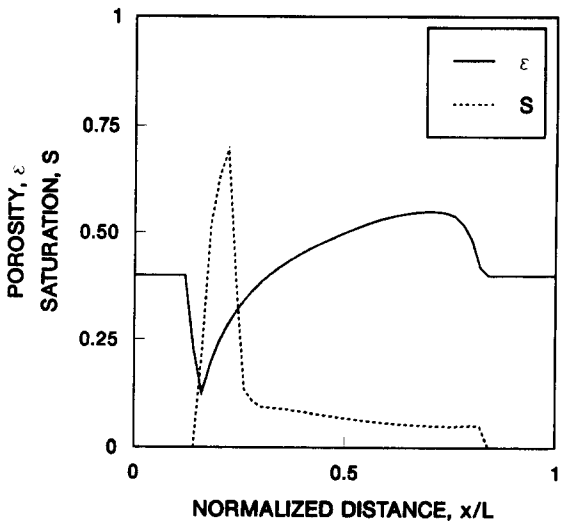

Figure 12 Porosity and saturation profiles at $t=2750$ s for a bed with an average particle diameter of 5.0 mm (for this calculation $L=0.5$ m)

two-phase (solid–liquid) molten pool. Above this pool, in region A, the saturation remains near the residual saturation, S_r.

Plots of UO_2 and ZrO_2 liquid fractions as functions of time are presented in Figure 10. After 3500 s have elapsed, two-thirds of the ZrO_2 is liquid while one-third of the UO_2 has melted. The ZrO_2 initially melts faster because the ZrO_2 liquid concentration is larger than the ZrO_2 solid concentration in the UO_2-rich regime (see Figure 2). Melt formation slows between 2510 s and 2780 s. During this time, liquid is relocating downward and freezing, forming a crust with a thickness on the order 10 cm (see Figure 8). After a lower blockage forms at $t=2780$ s, freezing slows considerably (a relatively small amount of liquid continues to freeze in the upper crust) and the rate of melting increases. As ZrO_2 in the solid is depleted, the ZrO_2 melting rate again decreases. At $t=3500$ s, half of the solid ZrO_2 is in the crusted and unaffected regions above and below the melt zone.

Because of the aforementioned preferential melting of ZrO_2, deviations from the initially uniform composition profiles can occur. Shown in Figure 11 are UO_2 and ZrO_2 volume fractions normalized by their initial values at $t=3000$ s. Both the ZrO_2 and UO_2 are depleted in the center of the bed while they accumulate in the upper and lower crusted regions. Only 15% of the UO_2 has melted at $t=3000$ s and the volume fraction varies from 0.8 to 1.3 times its initial value. On the other hand, almost 50% of the ZrO_2 has melted and its normalized volume fraction varies from 0.46 in the region where melt first formed to over 2.3 in the lower crust. The ZrO_2 to UO_2 mass ratio changes from its initial uniform value of 0.1 to 0.06 in the melt zone and to 0.18 in the lower crust.

Sensitivity analysis

Particle diameter. Solutions were obtained for three particle diameters, $d_p=0.2$ mm, 1.0 mm, and 5.0 mm. All other parameters were held fixed at their base case values. Increasing d_p enhances radiation heat transfer in the bed, raising both the solid diffusivity, α_s, and the thermal boundary layer thickness, δ. Consequently, the location of initial melt formation moves 0.07 m towards the center of the bed as d_p is changed from 0.2 mm to 5.0 mm (see Table 3). Because the center is initially at a lower temperature than the top, changing d_p from 0.2 mm to 5.0 mm delays melt formation by 190 s.

The time delay between melt formation and initial relocation is 40 s for 5 mm particles and 220 s for 0.2 mm particles. This variance is due to the dependence of the critical saturation, S_r, on d_p. By definition, S_r measures the amount of liquid that must accumulate before macroscopic liquid motion is observed. Taking $\gamma=0.45$ N/m, $\varepsilon=0.4$ and $\rho_l=7500$ kg/m^3, correlations in the appendix give $S_r=0.35$ for $d_p=0.2$ mm, $S_r=0.1$ for $d_p=1$ mm, and $S_r=0.05$ for $d_p=5$ mm. When d_p is decreased, S_r increases because a greater amount of liquid can be trapped between the particles by surface tension effects. Therefore, a larger fraction of the solid must melt before liquid motion is observed in beds composed of small particles.

Porosity and saturation profiles at $t=2750$ s for $d_p=5$ mm and $d_p=0.2$ mm are shown in Figures 12 and 13, respectively. Capillary forces have little effect on the flow in a bed with 5 mm particles. Melt forms and runs downward under the action of gravity, creating a thick lower crust (the region $0.06\text{ m}<x<0.16\text{ m}$ in Figure 12). Behind the liquid front the saturation approximately equals the residual saturation.

Capillary forces, which tend to move liquid into regions of low porosity, are dominant in beds composed of small particles. Note from Figure 13 that the saturation tends to be higher in regions of low ε in a bed of 0.2 mm diameter particles. Also note that an upper crust begins forming before $t=2750$ s indicating the importance of capillarity in such a bed. Because melt flows very slowly in a bed with small particles ($\kappa\sim d_p^2$), the solid in the region $0.14\text{ m}<x<0.19\text{ m}$ in Figure 13 reaches

Table 3 Effect of varying the particle diameter on the base solution

	Particle diameter, d_p (mm)		
	0.2	1.0	5.0
Solid first melts at			
$t_m=$	2158 s	2215 s	2346 s
$x_m=$	0.42 m	0.40 m	0.35 m
Liquid motion begins	2377 s	2311 s	2387 s
Lower crust starts forming	2960 s	2510 s	2450 s
Maximum lower crust thickness	4.0 cm	9.0 cm	11.5 cm
Blockage develops below the melt zone	3130 s	2780 s	2710 s
Upper crust starts forming	2590 s	2700 s	—
Maximum upper crust thickness	2.5 cm	2.5 cm	—
Blockage develops above the melt zone	3160 s	—	—

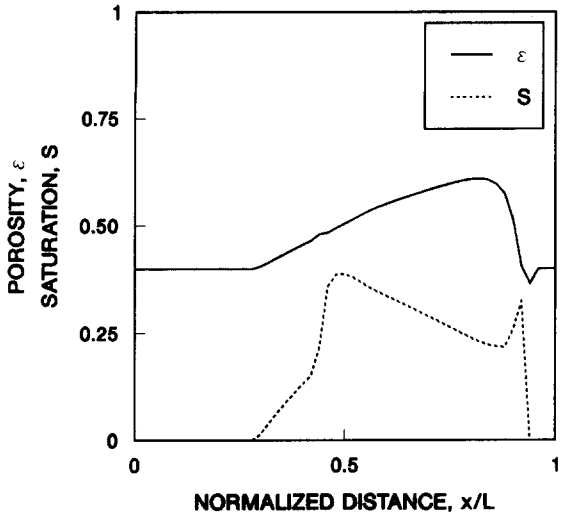

Figure 13 Porosity and saturation profiles at $t=2750$ s for a bed with an average particle diameter of 0.2 mm (for this calculation $L=0.5$ m)

the melting temperature before the arrival of the liquid front that is at $x=0.19$ m.

Bed height. Three bed depths were considered: 0.50 m, 0.75 m, and 1.00 m. From Table 4 it is evident that melt first forms at roughly the same distance from the top for all three cases. The top is the hottest initially and solid first melts at the edge of the upper thermal boundary layer ($L-\delta\simeq 0.1$ m). After the onset of melting, it takes 95 s for liquid to begin flowing and about 500 s elapse before an upper crust forms. In all three cases, the maximum thickness of the upper crust is 2.5 cm. Upward motion of liquid is independent of L because melt forms close to the top of the bed.

However, downward flow is highly dependent on L: the thickness of the lower crust increases rapidly until a flow blockage occurs and the maximum thickness increases linearly with L. The blockage forms at approximately the same distance from the bottom in all three cases; its location is determined only by the bottom boundary layer thickness. Consequently, less time elapses between initial melt formation and the creation of a blockage as L decreases.

Initial composition. Zirconia to urania mass ratios of 0.1, 0.2, and 0.3, corresponding to initial ZrO_2 volume fractions of 0.15, 0.25, and 0.35, respectively, were considered. Decreasing the UO_2 concentration reduces the decay heating and lowers the melting temperature (see Figure 2). Because the melting temperature is only weakly dependent on ZrO_2 mole fractions for mole fractions above 0.1 (mass ratios above 0.05), the reduction in heat release dominates the timing of initial melt formation. Note from Table 5 that melt formation is delayed by several hundred seconds as the ZrO_2 to UO_2 mass ratio increases from 0.1 to 0.3.

Flow characteristics remain relatively unaffected. After initial melt formation, approximately 100 s elapse before S reaches S_r, a crust starts forming 300 s later and a lower blockage occurs after 600 s in all three cases.

Normalized ZrO_2 to UO_2 mass ratios are shown in Figure 14 for an initial ratio of 0.1 at 2750 s (case i), an initial ratio of 0.2 at 3000 s (case ii) and an initial ratio of 0.3 at 3250 s (case iii). Different times were chosen for these plots to insure that the same amount of solid, approximately 10%, had melted in each case. Increasing the ZrO_2 concentration reduces the deviations from the initial uniform composition profiles. Because the composition of the initial melt is only weakly dependent on the ZrO_2 concentration (see Figure 2), the difference between ZrO_2 solid and liquid concentrations decreases as the initial ZrO_2 mass fraction is increased.

Initial conditions. Except in narrow thermal boundary layers, the temperature at a given location increases linearly with time. Consequently, the timing of initial melt formation is sensitive to the initial conditions. In the calculation discussed here the bed had an initial uniform temperature of 1500 K and both the top and the bottom continued to radiate to environments at 1500 K as temperatures in the bed increased—all other parameters were the same as those for the base case. Most of the bed heated isothermally at a rate of 0.43 K/s until significant liquid motion was observed ($t\simeq 3200$ s)—this heating rate is in excellent agreement with the predictions of Equation 9.

A schematic of crust growth for this bed is given in Figure 15. The porosity profiles are symmetric until $t\simeq 3300$ s, when a bottom crust begins forming. Because much of the bed reaches the melting temperature (which is slightly greater than 2800 K) simultaneously, the maximum lower crust thickness is small, on the order of 4 or 5 cm. Recall that when an initial linear temperature profile ranging from 1500 K at the bottom to 2000 K at the top was prescribed, the maximum crust thickness was 9 cm.

Conclusions

A model of melt formation and relocation is one-dimensional core rubble beds was developed in this study. The analysis

Table 4 Effect of varying the bed depth on the base case solution

	Bed depths, L (m)		
	0.5	0.75	1.00
Solid first melts at			
$t_m=$	2215 s	2126 s	2081 s
$x_m=$	0.40 m	0.64 m	0.88 m
Liquid motion begins	2311 s	2222 s	2176 s
Lower crust starts forming	2510 s	2470 s	2430 s
Maximum lower crust thickness	9.0 cm	15.0 cm	20.0 cm
Blockage develops below the melt zone	2780 s	2790 s	2870 s
Upper crust starts forming	2700 s	2630 s	2600 s
Maximum upper crust thickness	2.5 cm	2.5 cm	2.5 cm
Blockage develops above the melt zone	—	—	—

Table 5 Effect of the initial composition on the base solution

	Initial ZrO_2 to UO_2 mass ratio		
	0.1	0.2	0.3
Solid first melts at			
$t_m=$	2215 s	2400 s	2603 s
$x_m=$	0.40 m	0.39 m	0.39 m
Liquid motion begins	2311 s	2505 s	2721 s
Lower crust starts forming	2510 s	2730 s	2940 s
Maximum lower crust thickness	9.0 cm	9.5 cm	9.5 cm
Blockage develops below the melt zone	2780 s	3000 s	3260 s
Upper crust starts forming	2700 s	2880 s	3200 s
Maximum upper crust thickness	2.5 cm	2.5 cm	2.5 m
Blockage develops above the melt zone	—	—	—

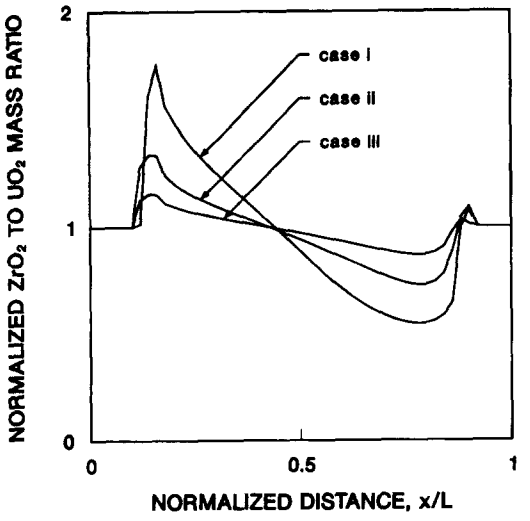

Figure 14 Zirconia to urania mass ratio normalized by its initial uniform value as a function of position for an initial ratio of 0.1 at $t=2750$ s (case i), an initial ratio of 0.2 at $t=3000$ s (case ii) and an initial ratio of 0.3 at $t=3250$ s (case iii) (for these calculations $L=0.5$ m)

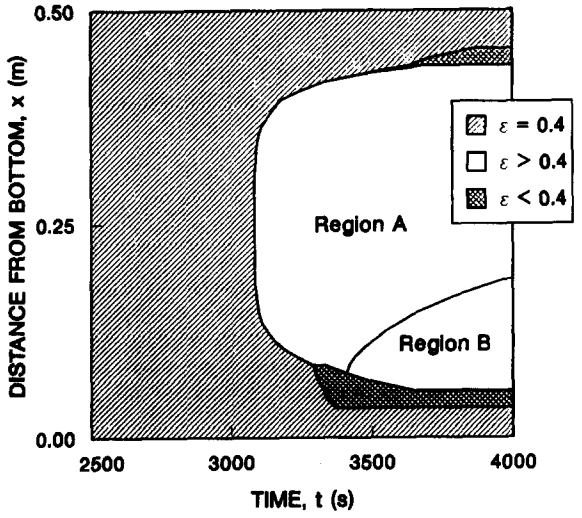

Figure 15 Schematic of crust growth for a bed initially at a uniform temperature of 1500 K. Region *B* consists of solid and liquid while region *A* is composed of solid, liquid and gas (that is, region *B* is filled with liquid)

included mass conservation equations for the species of interest (UO_2 and ZrO_2); a momentum equation which represented a balance among drag, capillary and gravity forces; an energy equation which incorporated the effects of convection by the melt, radiation and conduction through the bed and internal heat generation; and a UO_2-ZrO_2 phase diagram.

A few key results are that (1) capillary forces are only important in beds composed of particles smaller than a few millimeters in diameter and in such beds, melt relocates both upward and downward until it freezes, forming crusted regions above and below the melt zone; (2) as melt flows downward and freezes, a flow blockage forms near the bottom of the bed and the location of this blockage is determined by the bottom thermal boundary layer thickness; (3) the maximum thickness of the lower crust increases linearly with the height of the bed; and (4) deviations from the initially uniform composition profiles occur because ZrO_2 is preferentially melted and these deviations decrease as the initial ZrO_2 concentration is increased.

The need for experiments to help guide future theoretical work and to test the current models cannot be underemphasized. A few experiments[14] conducted in a research reactor provide some insight into the important physical processes. However, these experiments only provide an end-state and are not suitable for direct comparisons.

Acknowledgments

This work was supported by the United States Nuclear Regulatory Commission and was performed at Sandia National Laboratories, which is operated for the U.S. Department of Energy under contract number DE-AC04-76DP00789.

References

1 Tolman, E. L. *TMI-2 Accident Scenario Update*, EGG-TMI-7489, Idaho National Engineering Laboratory, Idaho Falls, ID, 1986

2 Lipinski, R. J. A particle-bed dryout model with upward and downward boiling, review of debris coolability models. *Trans. Am. Nuc. Soc.* 1980, **35**, 358–360

3 Ogniewicz, Y. and Tien, C. L. Analysis of condensation in porous insulation. *Int. J. Heat Mass Transfer* 1981, **24**, 421–429

4 Sahota, M. S. and Pagni, P. J. Heat and mass transfer in porous media subject to fires. *Int. J. Heat Mass Transfer* 1979, **22**, 1069–1081

5 Huang, C. L. D. Multi-phase moisture transfer in porous media subjected to temperature gradient. *Int. J. Heat Mass Transfer* 1979, **22**, 1295–1307

6 Nasrallah, S. B. and Perre, P. Detailed study of a model of heat and mass transfer during convective drying of porous media. *Int. J. Heat Mass Transfer* 1988, **31**, 957–967

7 Plumb, O. A., Spolek, G. A., and Olmstead, B. A. Heat and mass transfer in wood during drying. *Int. J. Heat Mass Transfer* 1985, **28**, 1669–1678

8 Lipinski, R. J. A coolability model for postaccident nuclear reactor debris beds. *Nuclear Technology* 1984, **65**, 53–66

9 Motakef, S. and El-Masri, M. A. Simultaneous heat and mass transfer with phase change in porous slab. *Int. J. Heat Mass Transfer* 1986, **29**, 1503–1512

10 Fey, Y. C. and Boles, M. A. The parametric analysis of self-freezing in an initially wet porous medium. *Int. J. Heat and Fluid Flow* 1988, **9**, 147–155

11 Weaver, J. A. and Viskanta, R. Melting of frozen, porous media contained in a horizontal or a vertical, cylindrical capsule. *Int. J. Heat Mass Transfer* 1986, **29**, 1943–1951

12 Chellaiah, S. and Viskanta, R. Freezing of saturated and superheated liquid in porous media. *Int. J. Heat Mass Transfer* 1988, **31**, 321–330

13 Beckermanm, C. and Viskanta, R. Natural convection solid/liquid phase change in porous media. *Int. J. Heat Mass Transfer* 1988, **31**, 35–46

14 Hitchcock, J. T. and Kelly, J. E. Post-test examinations of the in-pile molten pool experiments. *Trans. Am. Nucl. Soc.* 1982, **43**, 515

15 Scheidegger, A. E. *The Physics of Flow Through Porous Media*, 3rd ed., University of Toronto Press, Toronto, 1974, 266–290

16 Kelly, J. E., Henniger, R. J., and Dearing, J. F., *MELPROG-PWR/MOD1 Analysis of a TMLB Accident Sequence*, NUREG/CR-4742, SAND86-2175, Sandia National Laboratories, Albuquerque, NM, 1987

17 Hagrman, D. L. *MATPRO-Version 11 (Revision 2): A Handbook of Material Properties for Use in the Analysis of Light Water Reactor Fuel Rod Behavior*, NUREG/CR-0479, Idaho National Engineering Laboratory, Idaho Falls, ID, 1981

18 Bird, R. B., Stewart, W. E., and Lightfoot, E. N. *Transport Phenomena*, Wiley, New York, 1960, 199

19 Leverett, M. C. Capillary behavior in porous solids. *Pet Trans. AIME* 1941, **142**, 152–169

20 Batchelor, G. K. *An Introduction to Fluid Dynamics*, Cambridge University Press, Cambridge, 1967, 67

21 Brown, G. G. *Unit Operations*, 6th ed., Wiley, New York, 1956, 210–228

22 El-Wakil, M. M. *Nuclear Heat Transport*, International Textbook, New York, 1971, 94–98

23 Golden, D. W. *et al. TMI-2 Standard Problem Package*, EGG-TMI-7382, Idaho National Engineering Laboratory, Idaho Falls, ID, 1986

24 Hagrman, D. L. *Material Property Models for Severe Core Damage Analysis*, EGG-CDD-5801, Idaho National Laboratory, Idaho Falls, ID, 1982

25 Patankar, S. V. *Numerical Heat Transfer and Fluid Flow*, McGraw-Hill, New York, 1980

26 Reed, A. W. *DCC-1/DCC-2 Degraded Core Coolability Analysis*, NUREG/CR-4390, SAND85-1967, Sandia National Laboratories, Albuquerque, NM, 1985

27 Hofmann, G. and Barleon, L. Reduced coolability of particle beds as a result of capillary effects at horizontal phase boundaries. *Proceedings of the International ANS/ENS Topical Meeting on Thermal Reactor Safety*, San Diego, California, February 2–6, 1986

28 Kelly, J. E. Heat transfer characteristics of dry porous particulate beds with internal heat generation. *ASME-JSME Thermal Engineering Joint Conference Proceedings*, Honolulu, Hawaii, 1983

29 Luikov, A. V., Shashkov, A. G., Vasiliev, L. L., and Fraiman, Yu. E. Thermal conductivity of porous systems. *Int. J. Heat Mass Transfer* 1968, **11**, 117

Appendix (Physical characteristics)

Bird *et al.*[18] derive the following relation for the permeability by modeling the porous solid as a bundle of capillary tubes:

$$\kappa=\frac{d_p^2\varepsilon^3}{150(1-\varepsilon)^2} \tag{A1}$$

where the factor of 150 is determined by matching the above correlation to experimental data.

Reed *et al.*[26] give for the relative permeability, κ_1:

$$\kappa_1=\begin{cases}\kappa S_e^3 & \text{for } S>S_r\\ 0 & \text{for } S\le S_r\end{cases} \tag{A2}$$

where $S_e=(S-S_r)/(1-S_r)$ and the residual saturation S_r is defined as the threshold value of saturation below which bulk liquid motion ceases.

Brown *et al.*[21] give for the residual saturation, S_r:

$$S_r=\frac{1}{86.3}\left[\frac{\gamma}{\kappa\rho_l g}\right]^{0.263} \tag{A3}$$

Thus, S_r varies with the ratio of surface tension γ to gravity. The dependence of S_r on the porous matrix is contained in the permeability κ.

Hofmann and Barleon[27] give the following relation for the Leverett function, J:

$$J=a(S_e+b)^{-c} \tag{A4}$$

where $a=0.38$, $b=0.014$, and $c=0.27$.

Radiation heat transfer in the bed is incorporated using a modified gas conductivity, $k_g^*=k_g+k_{rad}$.[28] That is, it is assumed that gas conduction and radiation act in parallel. Several researchers have proposed that $k_{rad}=4\varepsilon_r\sigma d_p T^3$, where ε_r is the emissivity of the solid and σ is the Stefan-Boltzmann constant.[28,29] Empirical correlations for k_{eff} in solid–gas systems are available in the literature.[28,29] However, in the current problem, three phases (solid, liquid, and gas) are present. In calculating, k_{eff}, the solid and the liquid are treated as a single component with a volume averaged thermal conductivity k_σ. For a single phase i, k_σ depends only on Y_{ij} and k_{ij}. The following correlation gives k_{eff}:[28]

$$k_{eff}=\psi k_g^*+\frac{1-\psi}{k_\sigma\omega+k_g^*(1-\psi)}k_\sigma k_g^* \tag{A5}$$

where $\omega=0.3\phi^{1.6}(k_\sigma/k_g^*)^{-0.044}$, $\psi=(\phi-\omega)/(1-\omega)$ and ϕ $(\equiv\varepsilon-\varepsilon S)$ is the volume fraction occupied by gas. In the limit of a gas volume fraction of zero, both ω and ψ approach zero and consequently, $k_{eff}=k_\sigma$. On the other hand, in the limit of a gas volume fraction of one, ψ approaches one and $k_{eff}=k_g^*$.